Title	ACTIVE CONTROL METHODS FOR DRAG REDUCTION IN FLOW OVER BLUFF BODIES (Generation-Sustenance Mechanism and Statistical Law of Turbulence)
Author(s)	Choi, Haecheon
Citation	数理解析研究所講究録 (2002), 1285: 84-91
Issue Date	2002-09
URL	http://hdl.handle.net/2433/42432
Right	
Type	Departmental Bulletin Paper
Textversion	publisher

数理解析研究所講究録 1285 巻 2002 年 84-91

ACTIVE CONTROL METHODS FOR DRAG REDUCTION IN FLOW OVER BLUFF BODIES

Haecheon Choi

School of Mechanical and Aerospace Engineering, Seoul National University, Seoul 151-742, Korea

ABSTRACT

In this paper, we present two successful results from active controls of flows over a circular cylinder and a sphere for drag reduction. The Reynolds number range considered for the flow over a circular cylinder is $40 \sim 3900$ based on the free-stream velocity and cylinder diameter, whereas for the flow over a sphere it is 10^5 based on the free-stream velocity and sphere diameter. The successful active control methods are a distributed (spatially periodic) forcing and a high-frequency (time periodic) forcing. With these control methods, the mean drag and lift fluctuations decrease and vortical structures are significantly modified. For example, the time-periodic forcing with a high frequency (larger than 20 times the vortex shedding frequency) produces 50% drag reduction for the flow over a sphere at $Re = 10^5$. The distributed forcing applied to the flow over a circular cylinder results in a significant drag reduction at all the Reynolds numbers investigated.

INTRODUCTION

The drag and noise increase very rapidly with increasing speed of vehicles. Therefore, control of flow over a bluff body for drag and noise reduction has been considered one of the major issues in fluid mechanics. In the present study, we consider two kinds of bluff-body flows: one is the flow over a circular cylinder and the other is the flow over a sphere. These two flows contain most of the characteristics observed in flows over two- and three-dimensional bluff bodies, respectively.

So far, many researchers have applied three kinds of control methods to flow over a bluff body: passive, active open-loop (i.e. non-feedback) and active feedback controls. Among them, we restrict our control method to a category of the active open-loop control method in this paper and consider two types of active open-loop control methods. The first is a time-periodic forcing whose frequency is either near the vortex shedding frequency (low-frequency forcing) or similar to or larger than the frequency corresponding to the shear-layer instability (high-frequency forcing). The second is a steady but distributed (i.e. spatially varying) forcing. These two control methods are applied to flows over a circular cylinder and a sphere, in order to investigate the control effect on the drag, lift and flow structures.

The Reynolds number ranges considered are $Re = u_\infty d/\nu = 40 \sim 3900$ for flow over a circular cylinder and $Re = u_\infty d/\nu = 425 \sim 10^5$ for flow over a sphere, respectively, where Re is the Reynolds number, u_∞ is the free-stream velocity, d is the cylinder or sphere diameter, and ν is the kinematic viscosity. For flow over a circular cylinder, numerical simulations are conducted for all the Reynolds numbers investigated. On the other hand, for flow over a sphere, numerical simulations are conducted at $Re = 425 \sim 3700$ and an experimental study is carried out at $Re = 10^5$.

NUMERICAL AND EXPERIMENTAL METHODS

Flow over a Circular Cylinder

Flow over a circular cylinder is studied at $Re = 40 \sim 140$ and 3900 using a numerical method. For $Re = 40 \sim 140$, the flow is laminar and thus no turbulence model is used. For $Re = 3900$, large eddy simulation with a dynamic subgrid-scale model (Germano et al. 1991; Lilly 1992) is carried out. The numerical method used is based on a fully implicit fractional step method (Choi and Moin 1994) in generalized coordinates with the second-order central difference scheme for the discretization of the spatial derivatives. The numbers of grid points used are $320 \times 120 \times 16$ (spanwise direction) for $Re = 40 \sim 140$ and $672 \times 160 \times 64$ (spanwise direction) for $Re = 3900$. Even though the base flows at $Re = 40 \sim 140$ are two-dimensional, the computations are carried out in three dimension because of the distributed forcing applied in the spanwise direction.

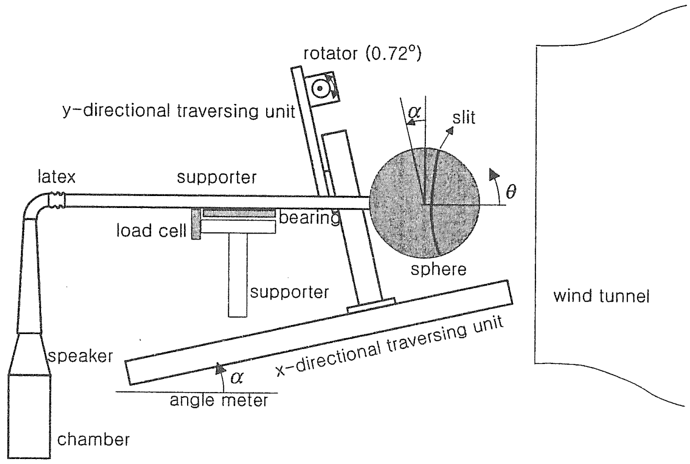

Figure 1. SCHEMATIC DIAGRAM OF THE EXPERIMENTAL SET-UP.

Table 1. FORCING CASES.

	Cylinder	Sphere
Low-frequency forcing	$Re = 100$ & 3900 (NUM)	$Re = 3700$ (NUM)
High-frequency forcing	$Re = 100$ & 3900 (NUM)	$Re = 3700$ (NUM) & 10^5 (EXP)
Distributed forcing	$Re = 40 \sim 140$ & 3900 (NUM)	$Re = 425$ (NUM)

Here NUM and EXP denote the numerical and experimental studies, respectively.

Flow over a Sphere

Flow over a sphere is studied at $Re = 425$ and 3700 using a numerical method and 10^5 using an experimental method, respectively.

For $Re = 425$, the flow is laminar unsteady and thus no turbulence model is used. For $Re = 3700$, large eddy simulation with a dynamic subgrid-scale model (Germano et al. 1991; Lilly 1992) is carried out. The numerical method used is based on a newly-developed immersed boundary method by Kim et al. (2001) with the second-order central difference scheme for the discretization of the spatial derivatives. The number of grid points used for $Re = 425$ is $449 \times 161 \times 40$, and that for $Re = 3700$ is $577 \times 141 \times 40$, respectively, in the streamwise, radial and circumferential directions.

For $Re = 10^5$, an experimental study is conducted. Figure 1 shows the schematic diagram of the present experimental set-up, consisting of an open-type wind tunnel, sphere, supporter, speaker, load cell and traversing unit. The diameter of a sphere is 150 mm, and the free-stream velocity is 10 m/s. A two-dimensional slit of 0.65 mm (about 0.5^o) width is located on the sphere surface at the angle of 76^o from the stagnation point, which is an upstream location of the separation line. A supporter attached to the sphere base is linked to a speaker chamber through latex. Then the speaker induces a time-periodic blowing and suction at a specified frequency at the slit. The forcing frequencies (f) applied are from 10 Hz to 370 Hz by increments of 10 Hz, corresponding to $St(= fd/u_\infty) = 0.15$ to 5.55 by increments of 0.15. For all the frequencies, the maximum velocity at the slit is tuned to be 1 m/s (10% of the free-stream velocity). The drag on the sphere is directly measured using a load cell (Cass BCL-1L), and the velocity field is measured with an in-house x-type hot-wire probe and a two-dimensional traversing unit that operates at variable horizontal angles. We also separately place a trip composed of two 0.5 mm-thick wires, respectively, at 55^o and 60^o to examine the effect of trip on the drag.

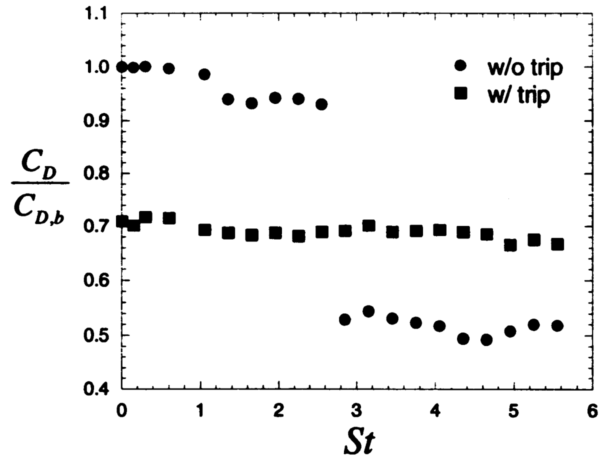

Figure 2. VARIATION OF THE DRAG COEFFICIENT WITH THE FORCING FREQUENCY.

CONTROL METHODS

The control methods used in this study are explained in this section: one is a time-periodic forcing and the other is a distributed forcing. For a time-periodic forcing, the disturbance is provided to the base flow either from the free-stream or from a slot on a bluff-body (cylinder or sphere) surface in a following manner:

$$\phi(t) = \alpha \sin(2\pi f t), \tag{1}$$

where t is the time, $\alpha(= 0.1u_\infty)$ is the forcing amplitude and f is the forcing frequency. The forcing frequency f is selected to be either near the vortex-shedding frequency (low-frequency forcing) or near or larger than the frequency corresponding to the shear-layer instability (high-frequency forcing).

For a distributed forcing, the disturbance is provided from a slot located on a bluff-body surface: for a cylinder

$$\phi(z) = \alpha \sin(2\pi \frac{z}{\lambda_z}) \tag{2}$$

and for a sphere

$$\phi(\theta) = \alpha \sin(m\theta), \tag{3}$$

where z is the spanwise direction of the cylinder, θ is the circumferential direction of the sphere, λ_z is the wavelength of the forcing in the spanwise direction, and m is an integer ($m = 1, 2, \cdots$).

RESULTS

Table 1 illustrates the forcing cases investigated in this study. In the below, we briefly describe the results from the controls listed in Table 1.

With low- and high-frequency forcings applied to the flows over a cylinder and a sphere were not successful in producing drag reduction at low Reynolds numbers ($< O(10^4)$) because the low-frequency forcing enhanced the vortex shedding and the high-frequency forcing increased the shear-layer instability after flow separation. On the other hand, the high-frequency forcing applied to the flow over a sphere at $Re = 10^5$ reduced the mean drag by 50%. This result will be described in more details later in this section.

The distributed forcing (spatially periodic forcing in the spanwise direction) was applied to the flow over a circular cylinder as shown in Table 1 with varying the forcing wavelength. With this control, the drag was significantly reduced when the base flow contained vortex shedding (i.e. $Re \geq 47$). This result will also be presented later in this section. Unlike the case of cylinder, the distributed forcing applied to the flow over a sphere slightly increased the drag for $m = 1, 2$ and 3 (Equation 3). This difference in the control results between the cases of the

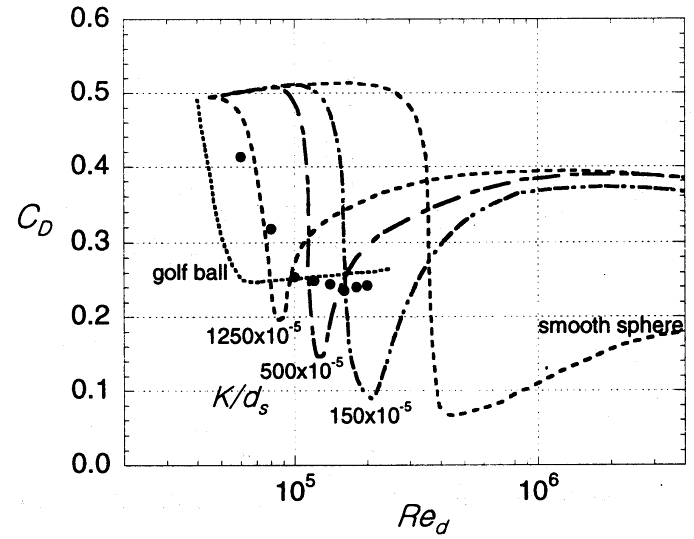

Figure 3. VARIATIONS OF THE DRAG COEFFICIENT DUE TO ACTIVE AND PASSIVE DEVICES AS A FUNCTION OF THE REYNOLDS NUMBER: •, PRESENT STUDY; DIMPLE (GOLF BALL), BEARMAN AND HARVEY (1976); ROUGHNESS (K), ACHENBACH (1974).

cylinder and sphere is mainly attributed to the very different vortical structures between two flows, indicating a significant dependence of the control method on the shape of a bluff body.

In the below, we present the results from two successful controls applied to the flows over a sphere and a cylinder.

Flow over a Sphere: High-Frequency Forcing at Re=10^5

Figure 2 shows the variations of the drag coefficient (C_D) with respect to the forcing frequency in the absence and presence of trip. Here the drag coefficient is normalized by that of the basic sphere (i.e. without forcing in the absence of trip; $C_{D,b}$) and $St = 0$ corresponds to the case of no forcing. The drag coefficient measured on the basic sphere is about 0.51, which is in good agreement with the result of Achenbach (1972). In the absence of trip, the drag abruptly decreases by about 50% at a critical forcing frequency of $St_c (= f_c d/u_\infty) = 2.85$ and becomes nearly constant for $St > St_c$. On the other hand, the drag is reduced by 30% in the presence of trip, but the forcing does not reduce the drag further. Strikingly, the amount of drag reduction from the forcing in the absence of trip is larger than that from the forcing in the presence of trip. The reason for this will be explained later in this section.

Figure 3 shows the variations of the drag coefficient due to active and passive devices as a function of the Reynolds number. It was shown in Achenbach (1974) that with surface roughness the drag coefficient rapidly decreases and then increases with increasing Reynolds number, showing a local minimum at a critical Reynolds number (Re_c). This critical Reynolds number decreases with increasing roughness. Also, the drag coefficient at $Re > Re_c$ increases more sharply at larger roughness and approaches 0.4. On the other hand, dimples reduce the drag coefficient even at a lower Reynolds number than surface roughness does (Bearman and Harvey 1976). After its decrease by dimples, the drag coefficient remains almost constant at about 0.25. In the present study, for different Reynolds numbers, we fix the forcing frequency to be $f = 330$ Hz ($fd/u_\infty = 4.95$ at $Re = 10^5$) and the forcing amplitude to be 1 m/s. It is shown in Figure 3 that the result of the present forcing is very similar to that with dimples. After its rapid decrease due to the present high-frequency forcing, the drag coefficient remains almost constant at about 0.24.

Figure 4 shows the surface-pressure distribution for different forcing frequencies in the absence of trip, together with those for the basic sphere and in the presence of trip, and the inviscid pressure (denoted as 'theoretical' in Figure 4). Unlike the cylinder, the base pressure itself does not contribute to the drag on the sphere because the area at the base point is zero. Considering the area, the pressures at the angles of 45^o and 135^o contribute most to the drag. At the forcing frequencies less than the critical forcing frequency ($St < St_c = 2.85$), the pressures on the sphere are similar to that on the basic sphere, indicating negligible or small drag reduction at these forcing frequencies. On the other hand, for the forcing frequencies larger than St_c, the surface pressures are nearly the same as the inviscid pressure for $\phi_s < 135^o$, indicating that a significant amount of drag reduction should occur

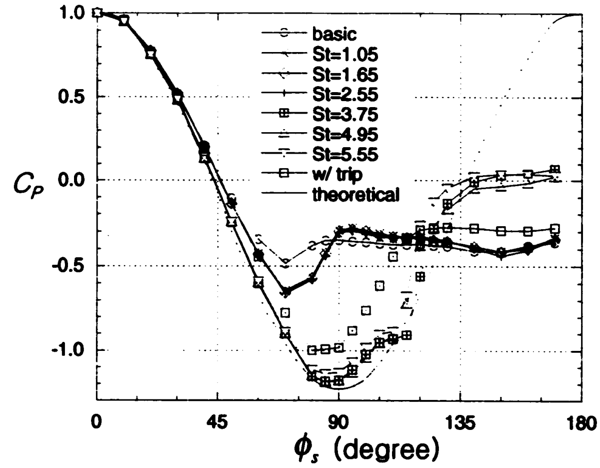

Figure 4. STATIC-PRESSURE DISTRIBUTION ON THE SPHERE SURFACE.

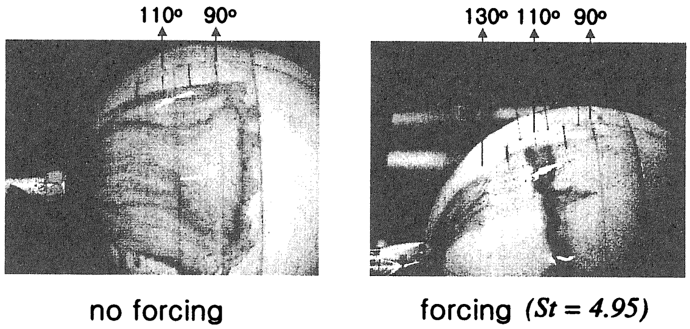

Figure 5. OIL FLOW PATTERN ON THE SPHERE SURFACE.

at these high forcing frequencies. Interestingly, the pressure on the tripped sphere surface approaches that of the very high frequency forcing at $\phi_s < 120^o$ but becomes nearly the same in the downstream surface as that on the basic sphere. It should be mentioned here that there exists a plateau in the pressure curve around 110^o for the high-frequency forcing cases ($St > 2.85$). This pressure pattern is very similar to that observed in the critical region where a separation bubble exists on the sphere surface (Achenbach 1974; Fage 1936; Suryanarayana and Meier 1995; Taneda 1978), suggesting an important clue to the present drag-reduction mechanism by the high-frequency forcing.

Figure 5 shows an oil flow visualization on the sphere. In the case of the basic sphere, separation occurs around 80^o, whereas for the case of $St = 4.95$ separation is delayed to occur at $105^o - 110^o$, and then the flow reattaches to the surface at $110^o - 115^o$, forming a separation bubble there. Second separation occurs near 130^o for $St = 4.95$. In the presence of trip (not shown here), separation occurred around 105^o and no separation bubble was observed near the sphere surface. Achenbach (1974) indicated that the low drag coefficient in the critical region is due to the existence of a separation bubble: with a separation bubble, reattached flow has high momentum near the wall with large turbulence intensity and thus delays second separation. The phenomenon occurred in the critical region of the basic sphere is very similar to the present observation, suggesting that large drag reduction achieved for $St > St_c$ is essentially due to the existence of the separation bubble. The existence of separation bubble was also confirmed from the velocity measurement near the sphere surface (not shown here).

Flow over a Circular Cylinder: Spatially Periodic Forcing

Figure 6 shows the schematic diagram of the forcing. Due to the fact that the forcing is applied in the spanwise direction, the controlled flow is three-dimensional even if the base flow is two-dimensional. Therefore, for $Re \leq 140$, the computational domain size in the spanwise direction is set to be the same as the wavelength of the forcing. In the case of turbulent flow ($Re = 3900$), the computational domain size of the controlled flow is the same as that of the uncontrolled flow. In this study, we have two different types of forcing: one is the in-phase forcing and the

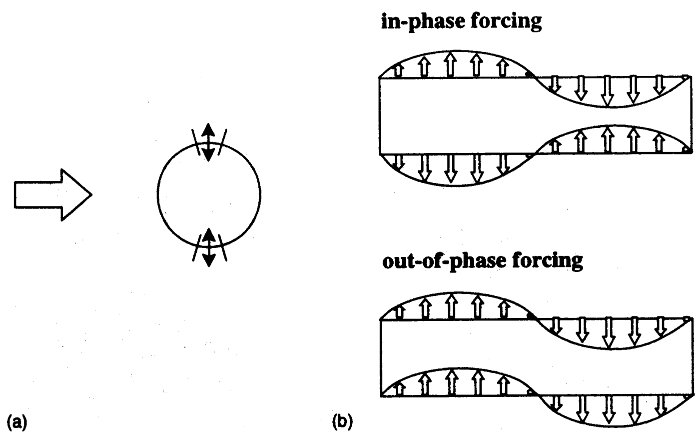

Figure 6. SCHEMATIC DIAGRAM OF THE DISTRIBUTED FORCING: (a) SIDE VIEW; (b) FRONT VIEW.

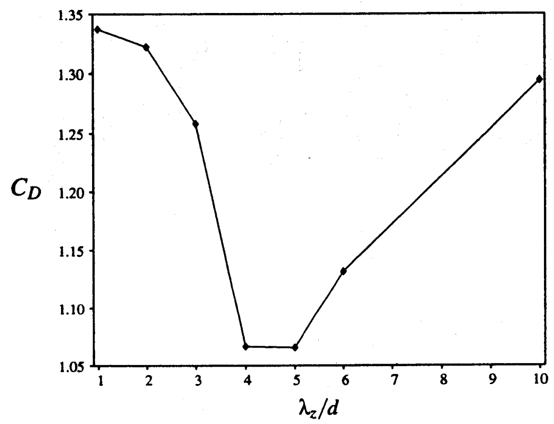

Figure 7. EFFECT OF THE IN-PHASE FORCING ON THE MEAN DRAG AT $Re = 100$.

other is the out-of-phase forcing (see Figure 6).

First, the in-phase forcing is applied to the flow over the cylinder at $Re = 100$. Figure 7 shows the variation of the drag coefficient with respect to the forcing wavelength ($\lambda_z = 1 \sim 10d$). The drag is minimum at $\lambda_z \approx 5d$, resulting in about 20% drag reduction. We have also applied the in-phase forcing to the flows at $Re = 80$ and 140. In these cases, the minimum drag occurred at $\lambda_z \approx 6d$ and $4d$, respectively, indicating that the optimum wavelength of the forcing decreases with increasing Reynolds number. It is interesting to note that the optimum wavelength is similar to the spanwise wavelength of the mode-A instability (Williamson 1996). The same in-phase forcing is applied to the flow at $Re = 40$, where there occurs no vortex shedding in the case of no forcing. In this case, there is nearly no change in the drag with the forcing, even though three dimensional flow structure appears in the wake due to the forcing.

Figure 8 shows the variation of vortical structures at $Re = 100$ (using the vortex identification method by Jeong and Hussain 1995) with the forcing wavelength. It is clear that at the optimum wavelength ($\approx 5d$) the flow becomes completely steady. The same observation was made for $Re = 80$. However, for $Re = 140$, the vortical structures were still unsteady even at the optimum wavelength owing to the strong vortex strength shed behind the cylinder at this Reynolds number.

Second, the out-of-phase forcing with $\lambda_z = 5d$ is applied to the flow over the cylinder at $Re = 100$. Figure 9 shows the instantaneous vortical structures for the out-of-phase forcing. Unlike the in-phase forcing, the flow with the out-of-phase forcing shows a clear vortex shedding, resulting in nearly no change in the drag as compared to that of the base flow.

Lastly, the in-phase and out-of-phase forcings are applied to the flow at $Re = 3900$. Here the base flow is three-dimensional and turbulent after separation. The size of the computational domain in the spanwise direction is πd, and the forcing wavelength is taken to be the same as the domain size. Figure 10 shows the variation of

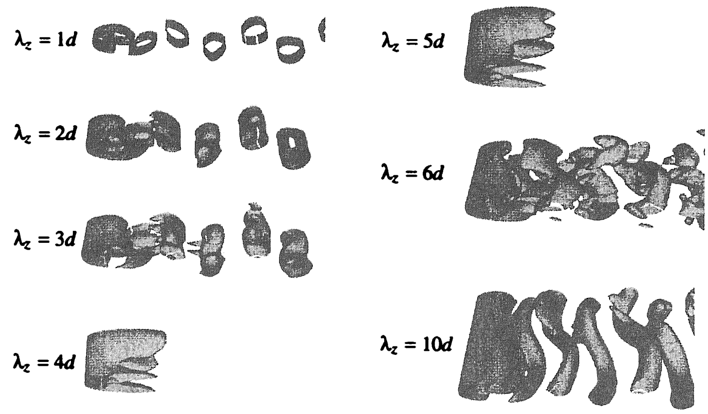

Figure 8. VARIATION OF VORTICAL STRUCTURES WITH THE FORCING WAVELENGTH AT $Re = 100$.

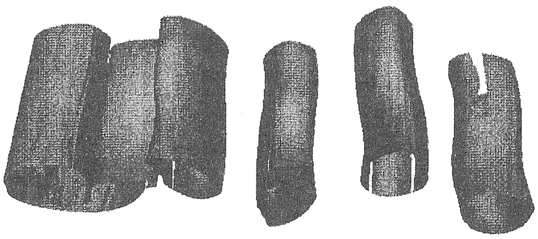

Figure 9. INSTANTANEOUS VORTICAL STRUCTURES FOR THE OUT-OF-PHASE FORCING ($\lambda_z = 5d$) AT $Re = 100$.

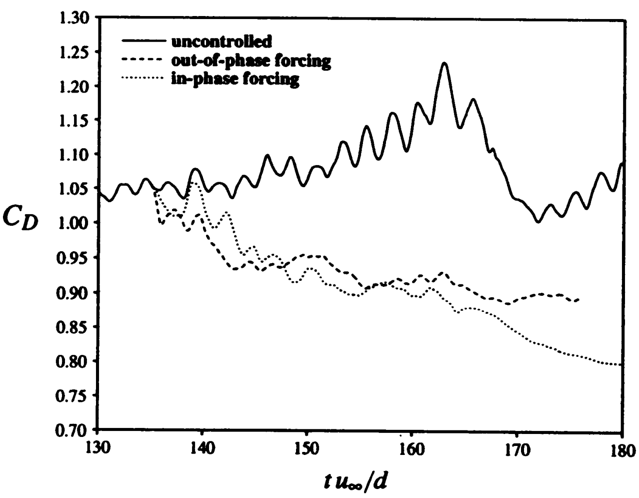

Figure 10. VARIATION OF THE DRAG COEFFICIENT DUE TO THE DISTRIBUTED FORCING AT $Re = 3900$.

the drag coefficient owing to the forcing. Surprisingly, the out-of-phase forcing as well as the in-phase forcing reduces the drag significantly. Instantaneous vortical structures for the base flow and flows with the forcing are shown in Figure 11. In the case of the out-of-phase forcing, the vortical structures are significantly changed near the separation point but those in the further downstream are similar to those of the base flow. On the other hand, the in-phase forcing drastically changes the vortical structures, showing almost no vortex right behind the cylinder and further delay of vortex shedding in the downstream.

CONCLUSION

In this paper, we presented the results from both the numerical and experimental studies on active control of flows over a circular cylinder and a sphere for drag reduction. The Reynolds number range considered for the flow

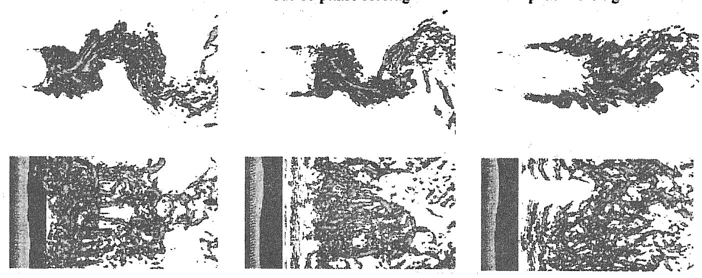

Figure 11. CHANGES IN THE INSTANTANEOUS VORTICAL STRUCTURES DUE TO THE DISTRIBUTED FORCING AT $Re =$ 3900.

over a circular cylinder was $100 \sim 3900$ based on the free-stream velocity and cylinder diameter, whereas for the flow over a sphere it was $100 \sim 10^5$ based on the free-stream velocity and sphere diameter. The active control methods investigated were (1) a forcing with a low frequency near the vortex shedding frequency; (2) a forcing with a high frequency that is much larger than the vortex shedding frequency; (3) a distributed (i.e. spatially varying) forcing. The control method (1) increased the mean drag and lift fluctuations at all the Reynolds numbers investigated for both flows. The result of the control method (2), however, showed a significant dependence on the Reynolds number. For example, a forcing with a high frequency (larger than 20 times the vortex shedding frequency) produced 50% drag reduction for the flow over a sphere at $Re = 10^5$, but increased the drag at Re=3700. The control method (3) applied to the flow over a circular cylinder resulted in a significant drag reduction for flow over a circular cylinder at all the Reynolds numbers investigated, but did not reduce the drag for the flow over a sphere, mainly because of the very different vortical structures between the flows over a sphere and a circular cylinder, showing a significant dependence of the control method on the shape of a bluff body.

ACKNOWLEDGMENT

This work is supported by the Korean Ministry of Science and Technology through the National Creative Research Initiatives.

REFERENCES

Achenbach, E.: Experiments on the flow past spheres at very high Reynolds numbers. J. Fluid Mech. 54, 565 (1972).

Achenbach, E.: The effect of surface roughness and tunnel blockage on the flow past spheres. J. Fluid Mech. 65, 113 (1974).

Bearman, P. W. and Harvey, J. K.: Golf ball aerodynamics. Aeronautical Quarterly May, 112 (1976).

Choi, H. and Moin, P.: Effects of the computational time step on numerical solutions of turbulent flow. J. Comp. Phys. 113, 1 (1994).

Fage, A.: Experiments on a sphere at critical Reynolds numbers. Aero. Res. Counc. R. & M. no. 1766, (1936).

Germano, M., Piomelli, U., Moin, P. and Cabot, W. H.: A dynamic subgrid-scale eddy viscosity model. Phys. Fluids A 3, 1760 (1991).

Jeong, J. and Hussain, F.: On the identification of a vortex. J. Fluid Mech. 285, 69 (1995).

Kim, J., Kim, D. and Choi, H.: An immersed-boundary finite volume method for simulations of flow in complex geometries. J. Comput. Phys. 171, 132 (2001).

Lilly, D. K.: A proposed modification of the Germano subgrid-scale closure method. Phys. Fluids A 4, 633 (1992).

Suryanarayana, G. K. and Meier, G. E. A.: Effect of ventilation on the flow field around a sphere. Exp. Fluids 19, 78 (1995).

Taneda, S.: Visual observations of the flow past a sphere at Reynolds number between 10^4 and 10^6. J. Fluid Mech. 85, 187 (1978).

Williamson, C. H. K.: Three-dimensional wake transition. J. Fluid Mech. 328, 345 (1996).